

An Energy Compartment Model for Propagation, Nonlinear Interaction, and Dissipation of Internal Gravity Waves

CARSTEN EDEN

Institut für Meereskunde, Universität Hamburg, Hamburg, Germany

DIRK OLBERS

Alfred-Wegener-Institut für Polar und Meeresforschung, Bremerhaven, Germany

(Manuscript received 11 October 2013, in final form 24 April 2014)

ABSTRACT

The recently proposed Internal Wave Dissipation, Energy and Mixing (IDEMIX) model, describing the propagation and dissipation of internal gravity waves in the ocean, is extended. Compartments describing the energy contained in the internal tides and the near-inertial waves at low, vertical wavenumber are added to a compartment of the wave continuum at higher wavenumbers. Conservation equations for each compartment are derived based on integrated versions of the radiative transfer equation of weakly interacting waves. The compartments interact with each other by the scattering of tidal energy to the wave continuum by triad wave-wave interactions, which are strongly enhanced equatorward of 28° due to parametric subharmonic instability of the tide and by scattering to the continuum of both tidal and near-inertial wave energy over rough topography and at continental margins. Global numerical simulations of the resulting model using observed stratification, forcing functions, and bottom topography yield good agreement with available observations.

1. Introduction

Internal tides and near-inertial waves can propagate and transport their energy over large distances in the ocean. On their way, they are refracted by the changing wave-supporting environment, and they interact with the background wave field, the mean flow, and topography. All these effects can lead to an energy transfer to short gravity waves, which are prone to vertical shear or convective instability, and therefore mix density in the interior ocean. This interior density mixing transfers the wave energy to large-scale potential energy and is thought to be an important driver of the ocean circulation (e.g., Wunsch and Ferrari 2004; Kunze and Smith 2004). To include this density mixing in ocean model components of comprehensive climate models—which are routinely used today to predict future climate—it becomes necessary to understand and to realistically simulate the generation and propagation of internal

tides and near-inertial waves in the ocean and in particular their interaction with shorter gravity waves and the final dissipation. A comprehensive overview of recent observational and modeling activities concerning internal tides, near-inertial waves, and internal waves in general can be found in St. Laurent et al. (2012) and references therein.

A promising concept for a model for the propagation and dissipation of internal waves both in the wavenumber–frequency domain and in physical space for the spectrum of weakly interacting waves was proposed by Müller and Briscoe (1999) and Müller and Natarov (2003). However, theoretical, practical, and numerical limits hamper the realization of such a comprehensive model of internal wave energetics. Olbers and Eden (2013) discussed a drastic simplification of the concept. Instead of resolving the whole wave spectrum as in Müller and Briscoe (1999) and Müller and Natarov (2003), they integrate the spectrum in the wavenumber–frequency domain, leading to conservation equations for integral energy compartments in physical space, which can be closed with a few simple but reasonable parameterizations. On the other hand, the integrated model in

Corresponding author address: Carsten Eden, Institut für Meereskunde, Universität Hamburg, Bundesstr. 53, 20146 Hamburg, Germany.
E-mail: carsten.eden@zmaw.de

the version by [Olbers and Eden \(2013\)](#) does not differentiate between internal tides, near-inertial waves, and the rest of the internal waves at higher frequencies and wavenumbers. It is the aim of this study to extend the model with energy compartments describing internal tides and near-inertial waves.

2. Wave continuum

The internal wave continuum at high vertical wavenumbers is treated as in [Olbers and Eden \(2013\)](#). The derivation is based on the radiative transfer balance equation of weakly interacting, internal gravity waves in the ocean ([Hasselmann 1968](#)). The interaction of the waves can in principle be expressed by a complicated scattering integral describing triad wave–wave interactions for which, however, no comprehensive parameterization exists up to now. In the closure by [Olbers and Eden \(2013\)](#), a few simple assumptions circumvent its specification. First, the total internal wave energy is split into the energy of upward- and downward-propagating waves by integrating over all negative and positive vertical wavenumbers and over all horizontal wavenumbers. Since wave–wave interactions conserve the energy of each interacting triad, the interaction integral drops from the compartment of total wave energy. It is then assumed that the dissipation of waves acts nearly symmetrically with respect to upward- and downward-propagating waves and that the effect of wave–wave interactions is to damp asymmetries in upward- and downward-propagating waves with a time scale τ_v on the order of days. The model by [Olbers and Eden \(2013\)](#) is then closed with a parameterization of the dissipation of internal wave energy based on a quadratic dependency on total wave energy ([Olbers 1976](#); [McComas and Müller 1981](#); [Gregg 1989](#)) and with a parameterization for the mean vertical group velocity of the wave field based on the observed shape of the internal wave spectrum, that is, the Garrett–Munk (GM) spectrum ([Cairns and Williams 1976](#); [Munk 1981](#)).

We follow [Olbers and Eden \(2013\)](#) in this treatment, but integrate the wave spectrum only over a vertical wavenumber range of the spectrum that excludes low modes, from m_ℓ to the rolloff wavenumber m_c , where the waves are increasingly subject to breaking since the vertical shear becomes large, such that the Richardson number related to the waves becomes approximately one. We call the compartment from m_ℓ to m_c the wave continuum. Energy fluxes due to refraction at m_ℓ are neglected for simplicity, since wave–wave and wave–topography interactions appear to be more important for the interaction of the different wave compartments. We also assume horizontally homogeneous conditions

for the wave continuum, and thus consider only the vertical energy propagation in Eq. (1) below. This is a reasonable assumption for the wave field in the high-wavenumber range, but for low wavenumbers lateral dispersion and lateral changes will play a more important role. Therefore, these waves are treated separately by introducing wave compartments for internal tidal waves and near-inertial waves.

The derivation of a conservation equation of the energy of the wave continuum E_c closely follows [Olbers and Eden \(2013\)](#) and is thus not repeated here. For time scales longer than the time scale τ_v for the symmetrization of the wave continuum, E_c evolves as

$$\partial_t E_c = \partial_z c_0 \tau_v \partial_z c_0 E_c - \mu f E_c^2 / c_\star^2 + W_c, \quad (1)$$

with the mean vertical group velocity c_0 of the upward- or downward-propagating waves. The parameter μ is $O(1)$, and c_\star is related to the bandwidth of the GM spectrum in wavenumber space. The main difference from the model by [Olbers and Eden \(2013\)](#) is the term W_c that denotes the interaction with the other wave compartments. It is specified below. The external forcing of the wave continuum enters as vertical boundary conditions for the flux $c_0 \tau_v \partial_z c_0 E_c$ in Eq. (1). It is given in the present study as a fraction of the conversion from barotropic to baroclinic tides at the bottom and the radiation of wind-driven near-inertial waves from the surface mixed layer (see below). Other forcing agents such as lee-wave generation of the geostrophically balanced flow or interaction of internal waves with surface waves may be included but are not considered here.

3. Low modes

For the small vertical wavenumbers, equivalent to the first few baroclinic modes, we apply the hydrostatic approximation. We consider a field of long gravity waves for a certain baroclinic mode n with dispersion relation $\omega^2 = f^2 + c_n^2 |\mathbf{k}|^2$, where the baroclinic gravity wave speed c_n can be approximated by $c_n \approx \int_{-h}^0 N / (n\pi) dz$ (see, e.g., [Olbers et al. 2012](#)). The energy spectrum E_n of the wave field can be specified as a function of the horizontal wavenumber vector \mathbf{k} , but also as a function of the frequency ω and the angle ϕ of the wavenumber vector $\mathbf{k} = |\mathbf{k}|(\cos\phi, \sin\phi)$. The spectrum $E_n(\mathbf{x}, \omega, \phi, t)$ is governed by the radiation transfer equation

$$\partial_t E_n + \mathbf{V} \cdot \mathbf{c}_g E_n + \partial_\phi \dot{\phi} E_n = W_n + T_n, \quad (2)$$

where $\partial_t c_n = 0$ was assumed for simplicity, which implies $\dot{\omega} = 0$ (this assumption can readily be relaxed). All vectors are horizontal in this study, that is, $\mathbf{V} = (\partial_x, \partial_y)$,

$\mathbf{x} = (x, y)$, and so on. The right-hand side of Eq. (2) describes the wave–wave interactions W_n and interaction with the topography T_n . For a fixed frequency as for a tidal constituent, we can drop ω as an argument and write $E_n = E_n(\mathbf{x}, \phi, t)$. The group velocity is related to the energy propagation in physical space and is given by

$$\mathbf{c}_g = \frac{\partial \omega}{\partial \mathbf{k}} = c_n \sqrt{\omega^2 - f^2} \omega^{-1} (\cos \phi, \sin \phi). \quad (3)$$

The change of angle ϕ is related to the refraction term in Eq. (2) and follows from $\cot \phi = k_x/k_y$ as

$$\dot{\phi} = \left(\frac{c_n}{\omega \sqrt{\omega^2 - f^2}} f \nabla f + \omega^{-1} \sqrt{\omega^2 - f^2} \nabla c_n \right) (\sin \phi, -\cos \phi). \quad (4)$$

The effect of $\dot{\phi}$ is to transport energy toward smaller c_n and smaller f . Given c_n and the right-hand side of Eq. (1), the radiation transfer equation for E_n can be integrated in time in (\mathbf{x}, ϕ) space. The lateral boundary condition for E_n is no flux in \mathbf{x} and specular reflection in ϕ at coastlines.

For a certain tidal frequency the energy is distributed over different baroclinic modes. To simplify the problem, we consider here compartments of tidal wave energy, for which the first few low modes are summed, which is equivalent to integrating the energy from the zero vertical wavenumber to m_ℓ , which is the wavenumber separating the low modes from the wave continuum. We assume that the ratio of the energy content of the tidal constituent in the different vertical modes stays approximately constant. To obtain the effective values of \mathbf{c}_g and $\dot{\phi}$ in the integrated version of Eq. (2), it is possible to follow the treatment of the mean vertical group velocities of the wave continuum as in Olbers and Eden (2013) by assuming a certain spectrum of the baroclinic modes. However, since we expect that the first baroclinic mode $n = 1$ will dominate the energy spectrum, we simply take \mathbf{c}_g and $\dot{\phi}$ as the respective properties for $n = 1$.

While the frequency ω for each tidal constituent is fixed, near-inertial waves are observed in the frequency band close to and slightly larger than the local f as they have been excited at higher latitudes and propagated southward. For the near-inertial wave energy, we therefore integrate the wave energy over vertical wavenumbers from 0 to m_ℓ , but also over the local near-inertial frequency band. Effective values of \mathbf{c}_g and $\dot{\phi}$ for the near-inertial waves may be obtained as indicated above for the tidal compartment. For simplicity, however, we use a local near-inertial frequency $\omega = 1.05f$ (see, e.g., Garrett 2001) and the first baroclinic mode for c_n . Furthermore,

we ignore details of the energy contained in the low modes for frequencies different from tides or near-inertial waves and rather assume that we can describe them by the present low-wavenumber compartments.

4. Wave–wave interaction

To couple the low-mode compartments $E_n(\mathbf{x}, \phi, t)$ with the wave continuum $E_c(\mathbf{x}, \phi, t)$, we need to know the vertical structure of E_n . The vertical structure of a gravity wave is given by its eigenfunction $\varphi_n(z)$, and the energy (local in z) of a long gravity wave is given by

$$\begin{aligned} \tilde{E}_n(\mathbf{x}, z, t) &= \Phi(z) \int_0^{2\pi} E_n(\mathbf{x}, \phi, t) d\phi, \\ \Phi(z) &= \frac{1}{2} \left[\left(1 + \frac{f^2}{\omega^2} \right) \frac{\varphi_n^2(z)}{c_n^2} + \left(1 - \frac{f^2}{\omega^2} \right) \frac{\varphi_n^2(z)}{N^2(z)} \right]. \end{aligned} \quad (5)$$

To calculate the eigenfunctions numerically, we use¹ the approximate form

$$\varphi_n(z) = A_n N^{1/2} \cos \int_{-h}^z N/c_n dz', \quad (6)$$

with the normalization $\int_{-h}^0 \varphi_n^2 c_n^{-2} dz = 1$ to determine the constant A_n .

Important for the model is the specification of the wave–wave interaction terms W_c and W_n . For the M_2 tidal constituent, we specify the wave–wave and topography interaction terms as

$$W_{M_2} + T_{M_2} = -\alpha_{M_2-c} E_{M_2} \int_{-h}^0 E_c dz - \tau_{M_2}^{-1} E_{M_2}. \quad (7)$$

The first term is quadratic in the wave energy and is derived from the scattering integral for the wave–wave interaction as detailed in the appendix. The coupling coefficient α_{M_2-c} is shown in Fig. 1. It is enhanced equatorward of about 28° because of the parametric subharmonic instability (PSI) of the internal M_2 tide. Note that the M_2 tide is subject to PSI everywhere between 28°S and 28°N, not only close to the critical latitude. This follows from our analysis of the wave–wave interaction integral as shown in the appendix. The second term is linear and describes the interaction with topography. Except near the coastline (see below), the time scale τ_{M_2} is derived from the scattering of internal waves over the rough abyssal hill topography to the

¹ To avoid a discrete derivative of φ , we use in fact for φ' the approximate form $\varphi'_n = A'_n N^{-1/2} \sin \int_{-h}^z N/c_n dz'$ with the (redundant) normalization $\int_{-h}^0 (\varphi'_n)^2 N^{-2} dz = 1$.

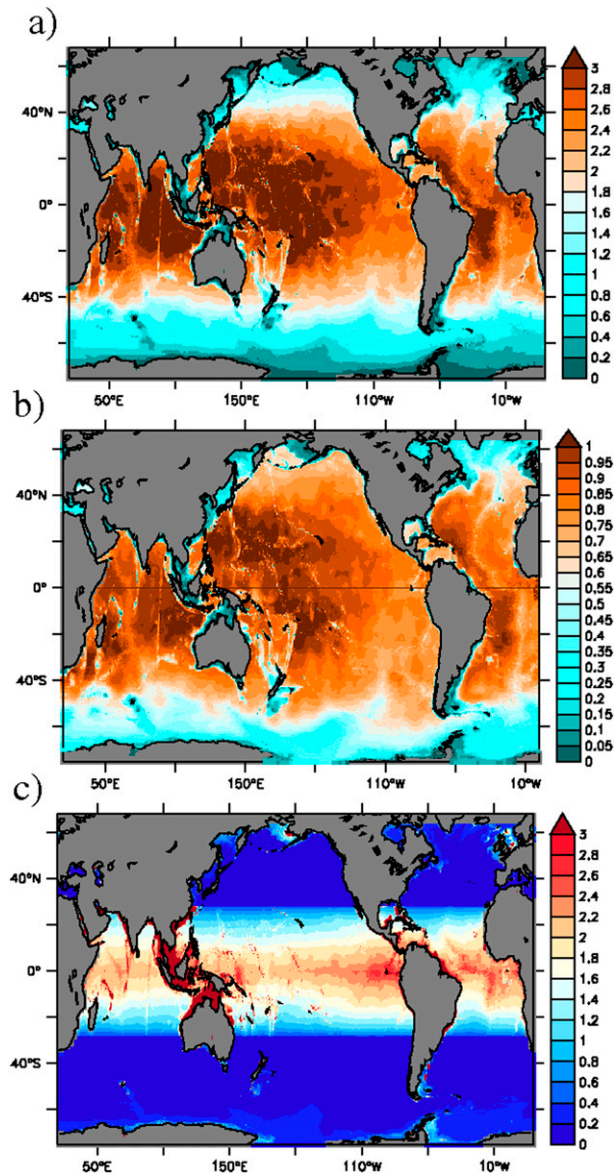


FIG. 1. (a) Group velocity $|c_g|$ of the M_2 internal tide (m s^{-1}). (b) The $|c_g|$ of near-inertial waves (m s^{-1}). (c) Coupling coefficient α_{M_2-c} (10^{-6} s m^{-3}). Note the different color scale in (a) and (b).

wave continuum as described by Müller and Xu (1992), which is also detailed in the appendix. The time scale τ_{M_2} is shown in Fig. 2a. The structure in τ_{M_2} in the interior is to a large extent related to the abyssal hill roughness represented by the variance h_{rms}^2 , which is in turn related to the spreading rate of the midoceanic ridge system and the sediment thickness as given by Goff and Arbic (2010) (see appendix).

A further effect of topography on low-mode gravity waves is given by scattering along the continental margins and isolated islands. Using a linear model, Kelly et al. (2013) estimated that on average 40% of the

incident energy of the low-mode internal M_2 tidal energy is reflected at the continental margin, while 40% is scattered to higher vertical modes and the rest is transmitted to the shelf. Since we are concerned with internal wave propagation in the interior of the ocean, the exact location of the reflection of the low modes, either at the continental margin or directly at the coastline, might be less important. The scattering to higher modes is, however, important for our purpose. Unlike for the scattering at rough topography, an analytical theory is not available that we could build on to describe this scattering effect. Therefore, we simply set the time scale τ_{M_2} at points closer than 300 km to the coastline to a value of 7 days. Such a time scale corresponds roughly to the time a wave with a group speed of 1 m s^{-1} needs to cross a shelf with a typical width of 300 km twice, such that the wave will decay by roughly 60% at the shelf using a decay time scale of this value. Since group speeds of the internal M_2 tide and near-inertial waves are in general smaller than 1 m s^{-1} (see Fig. 1), and the wave might not propagate perpendicularly toward the coastline, our approach appears to be an upper bound for the effect of scattering along the continental margins. We also discuss sensitivity experiments with smaller time scales than 7 days to estimate the effect of our choice.

The interaction of near-inertial waves (niw) with the wave continuum is found to be very small (see appendix), so that there is no need to specify a corresponding term. The treatment of the interaction with topography follows that of the M_2 tide. We therefore specify the interaction as

$$W_{\text{niw}} + T_{\text{niw}} = -\tau_{\text{niw}}^{-1} E_{\text{niw}}. \quad (8)$$

The time scale τ_{niw} is shown in Fig. 2b. To conserve energy we specify W_c as

$$W_c = \alpha_{M_2-c} \tilde{E}_{M_2} \int_{-h}^0 E_c dz + \tau_{M_2}^{-1} \tilde{E}_{M_2} + \tau_{\text{niw}}^{-1} \tilde{E}_{\text{niw}}. \quad (9)$$

5. Results

a. Model configuration

We use the hydrographic climatology by Gouretski and Koltermann (2004) to calculate $N^2(\mathbf{x}, z)$, c_n , and the eigenfunctions φ_n and φ'_n . As forcing for the internal waves, we use the flux from the barotropic to the internal M_2 tide derived by Nycander (2005) and the flux due to wind-driven, near-inertial waves in the mixed layer of the ocean from Rimac et al. (2013). Both forcing functions are shown in Fig. 3. We take 20% of the flux

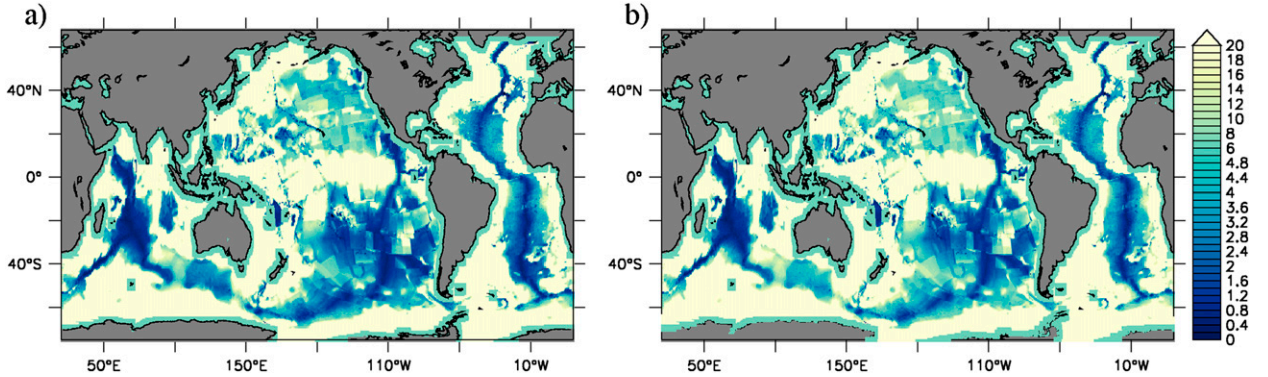


FIG. 2. Decay time scales (days) due to scattering at topography (a) τ_{M_2} and (b) τ_{niw} .

into near-inertial waves in the mixed layer as the amount radiating into the interior of the ocean. Such a ratio was also suggested by Jochum et al. (2013) based on results by Large and Crawford (1995) and Furuichi et al. (2008). After interpolation on our numerical grid, the globally integrated values are 0.75 and 0.09 TW for the bottom and surface forcing of the internal waves, respectively.

The internal wave continuum equation is solved with a fully implicit time stepping, except for the forcing W_c in Eq. (1) that is added using forward time stepping. The low-mode energy Eq. (2) is solved with forward time stepping and the positive definite Superbee scheme taken from the Massachusetts Institute of Technology General Circulation Model (Marshall et al. 1997) for advection in \mathbf{x} and ϕ , since this scheme provides the best results with respect to numerical diffusion and dispersion compared to other schemes that we have tested in idealized configurations. The horizontal and vertical resolution are the ones of the hydrographic climatology by Gouretski and Koltermann (2004), that is, $0.5^\circ \times 0.5^\circ$ and 44 vertical levels with thickness ranging from 10 m at the surface to 250 m below 1500 m. The time step is

$\Delta t = 1200$ s. The exchange term W_{M_2} is limited by $W_{M_2} = -\min(0.5/\Delta t, \alpha_{M_2-c} \int E_c dz) E_{M_2}$. This limiter conserves energy and is necessary for a stable integration, but is only active at a few grid points with very large α_{M_2-c} . The parameters τ_{M_2} and τ_{niw} are also limited to be larger than Δt , which is again necessary for a few grid points only.

In principle it is possible to obtain the forcing of the low modes as a function of the angle of the wave propagation ϕ [using, e.g., the method by Nycander (2005) in wavenumber space for the tides], but for simplicity it is here equally distributed in ϕ for both the tidal and the near-inertial wave component. We also have to specify the amount of energy injected into the low modes and into the wave continuum for both the tidal forcing at the bottom and the near-inertial wave forcing at the surface. For the tidal forcing, we inject the energy in equal parts to the tidal compartment and the wave continuum, following roughly the estimate of St. Laurent and Garrett (2002) and the treatment of the tidal energy forcing in the parameterization by Jayne (2009). We note that the fraction that is directed here to the wave continuum might be overestimated, since Falahat et al. (2014, manuscript submitted to *J. Phys. Oceanogr.*) report

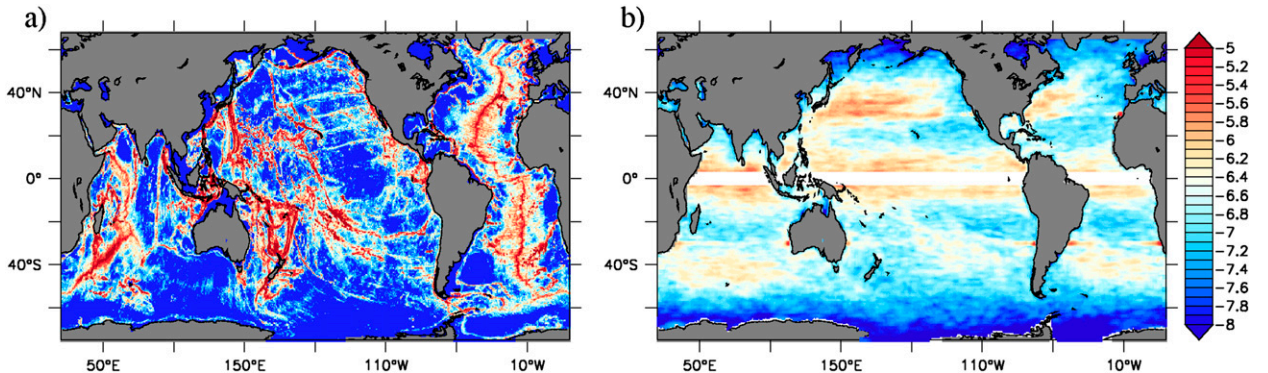


FIG. 3. (a) Tidal forcing and (b) near-inertial wave forcing [$\log_{10} F$ ($\text{m}^3 \text{s}^{-3}$) $^{-1}$].

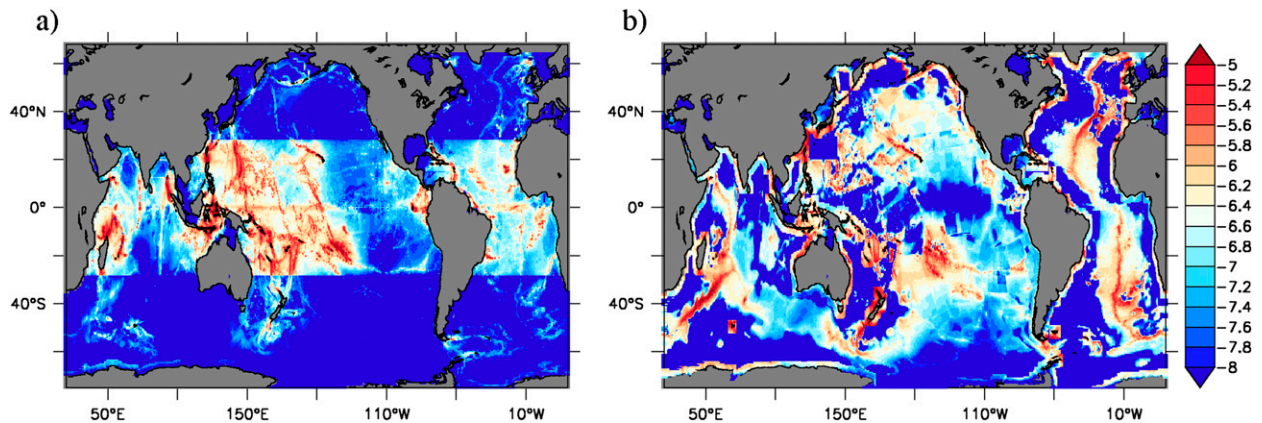


FIG. 4. (a) Dissipation of internal tide M_2 by wave–wave interaction with the continuum $\int_0^{2\pi} W_{M_2} d\phi$ and (b) scattering at rough topography and continental margins $\int_0^{2\pi} T_{M_2} d\phi$ [$\log_{10} F$ ($\text{m}^3 \text{s}^{-3}$) $^{-1}$].

a portion of 60%–70% of the globally averaged total flux that is transferred to the first 3 baroclinic modes and 70%–80% to the first 10 modes.

For the near-inertial waves, we inject all energy from the surface forcing function into the low modes. Since the flux is estimated using a hydrostatic model, which resolves only the first few vertical modes of gravity waves, this approach seems at least consistent, although we are aware that also higher vertical modes are involved in the near-inertial wind forcing. A complication for the near-inertial wave compartment and its forcing occurs at the equator, where the inertial period becomes singular and an adjustment of the theory is in principle needed. However, here we simply restrict the forcing of the near-inertial wave compartment to regions poleward of 3° latitude.

b. Tides and wave continuum

We start with an experiment coupling the M_2 tide and the wave continuum. The forcing of the wave field comes only from the barotropic tide as shown in Fig. 3a. After about 1 yr the model reaches an equilibrium. Figure 4 shows the energy transfer $\int_0^{2\pi} W_{M_2} d\phi$ due to triad wave–wave interaction and $\int_0^{2\pi} T_{M_2} d\phi$ due to scattering at rough topography from the M_2 tidal compartment to the wave continuum. The globally integrated energy transfer rates are $\int W_{M_2} d\phi dA = 0.17 \text{ TW}$ and $\int T_{M_2} d\phi dA = 0.2 \text{ TW}$. More than 90% of $\int W_{M_2} d\phi dA$ is obtained by integrating equatorward of 28° latitude, although this area is only 50% of the total area. Thus, almost all energy loss by the wave–wave interaction is due to parametric subharmonic instability. From the interaction with topography, 40% or 0.08 TW is due to scattering at the continental margins, the dominant part is due to scattering at rough topography in the interior of the ocean. The total dissipation of internal wave energy is 0.75 TW , which equals the total forcing.

Results of the simulation with respect to surface elevation ζ of the internal M_2 tide are shown in Fig. 5a together with observational estimates of ζ by Müller et al. (2012) in Fig. 5c on the same color scale. To obtain the surface elevation $\zeta = p_s/g$ of internal tides in the model, we calculate the surface pressure $p_s = p(z = 0)$ from the pressure amplitude related to the gravity waves from

$$p(z) = a\sqrt{\omega^2 - f^2}\omega^{-1}\varphi_n(z), \quad (10)$$

where the modulus of the amplitude a is given by $|a|^2 = \int_0^{2\pi} E_n d\phi$. Differences between the simulation and the observations can be seen in the western boundary currents and the Antarctic Circumpolar Current, but those signals in the observations are probably due to mesoscale eddy activity and are not internal tides. There is also a large signal stretching poleward from the Aleutian Archipelago toward Hawaii in the observations, which cannot be seen in the simulation due to a missing forcing at this position (cf. Fig. 3a). Overall, however, there is good agreement between observational estimates and the simulation. Figure 5e shows a recent compilation of energy levels at the M_2 tidal frequency in low vertical modes at several mooring sites by Alford and Zhao (2007), which can be compared with the simulated M_2 tidal energy in Fig. 5b. Although these observations are very sparse, the comparison demonstrates at least an agreement in the order of magnitude in the M_2 energy level.

Figures 6a and 6c show the vertical diffusivity K in the simulation, obtained by using the Osborn–Cox relation (Osborn and Cox 1972) as in Olbers and Eden (2013) to calculate $K = \delta/(1 + \delta)\mu f E_c^2 c_*^{-2} N^{-2}$, where $\delta = 0.2$ denotes a mixing efficiency. As expected, K is enhanced toward the bottom. It is large over rough topography

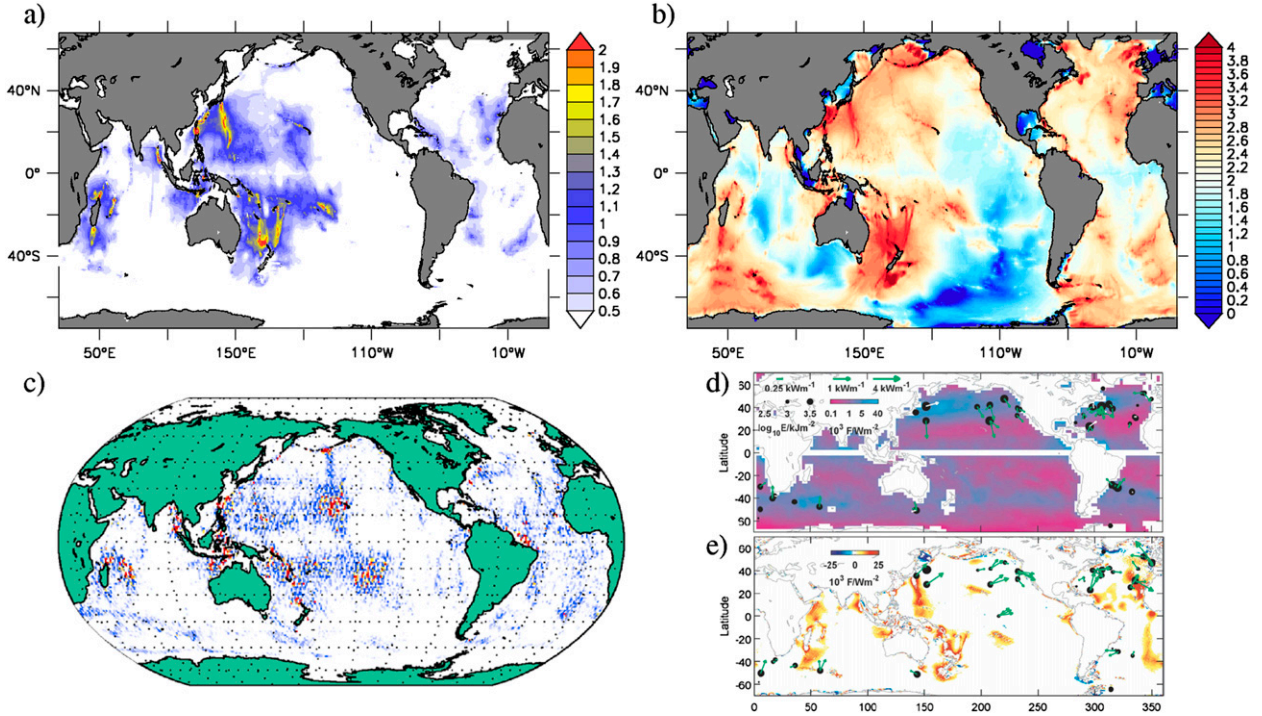


FIG. 5. (a) Equivalent surface elevation ζ (cm). (b) M_2 energy $[\log_{10} \int_0^{2\pi} E_{M_2} d\phi \text{ (J m}^{-2}\text{)}^{-1}]$. (c) Observed surface elevation ζ (m) taken from Müller et al. (2012) on the same color scale as in (a). (d) Dots represent observed energy levels in low-mode near-inertial waves taken from Alford and Zhao (2007); color shading indicates the near-inertial energy input. (e) Dots represent observed energy levels in low-mode M_2 tides taken from Alford and Zhao (2007).

and near locations with maxima in the tidal forcing. In regions with flat abyssal topography poleward of 28° latitude, K almost vanishes. Since K depends strongly on the stratification, it is more instructive to look at the dissipation. Although the forcing of the wave field is only at the bottom in this experiment, less than 30% (10%) of the total dissipation $\int \mu f E_c^2 c_\star^{-2} dV$ takes place below 1000-m (2000 m) depth and is related to the enhanced values of K . The horizontal location of this deep dissipation closely follows the pattern of K in Fig. 6c.

c. Near-inertial waves and wave continuum

We continue by considering an experiment where we couple the near-inertial wave compartment and the wave continuum. Forcing is only at the surface for the near-inertial wave compartment. After about 1 yr the model reaches an equilibrium. Figure 7 shows the energy level of the near-inertial waves and the exchange term $\int_0^{2\pi} T_{\text{niw}} d\phi$. The global integral of $\int T_{\text{niw}} d\phi dA$ equals the forcing of 0.09 TW. The scattering at the continental margins contributes to 30% or 0.03 TW to the total dissipation of near-inertial wave energy; the remainder is due to scattering at rough topography in the interior. Energy levels are of comparable magnitude as

the energy level, which is in agreement with the observational estimates by Alford and Zhao (2007) shown in Fig. 5e.

Figures 6b and 6d show the vertical diffusivity K in this simulation. Values are smaller than coupling the M_2 tide to the wave continuum, but are also bottom enhanced, although the forcing of the wave field is at the surface only. This is due to the vertical propagation and symmetrization of the wave continuum. It is interesting that K is enhanced at similar locations as in the experiment with tidal forcing only. This is because of similar horizontal propagation properties of the corresponding low modes and similar bottom scattering effects. Similar to the internal tide case, less than 30% (10%) of the total dissipation $\int \mu f E_c^2 c_\star^{-2} dV$ takes place below 1000-m (2000 m) depth.

6. Summary and discussion

A model for the propagation and dissipation of weakly interacting, internal gravity waves based on the six-dimensional (\mathbf{x} , z , \mathbf{k} , and m) radiative transfer equation, as suggested by Müller and Briscoe (1999) and Müller and Natarov (2003), remains too complex to be realized. The Internal Wave Dissipation, Energy and

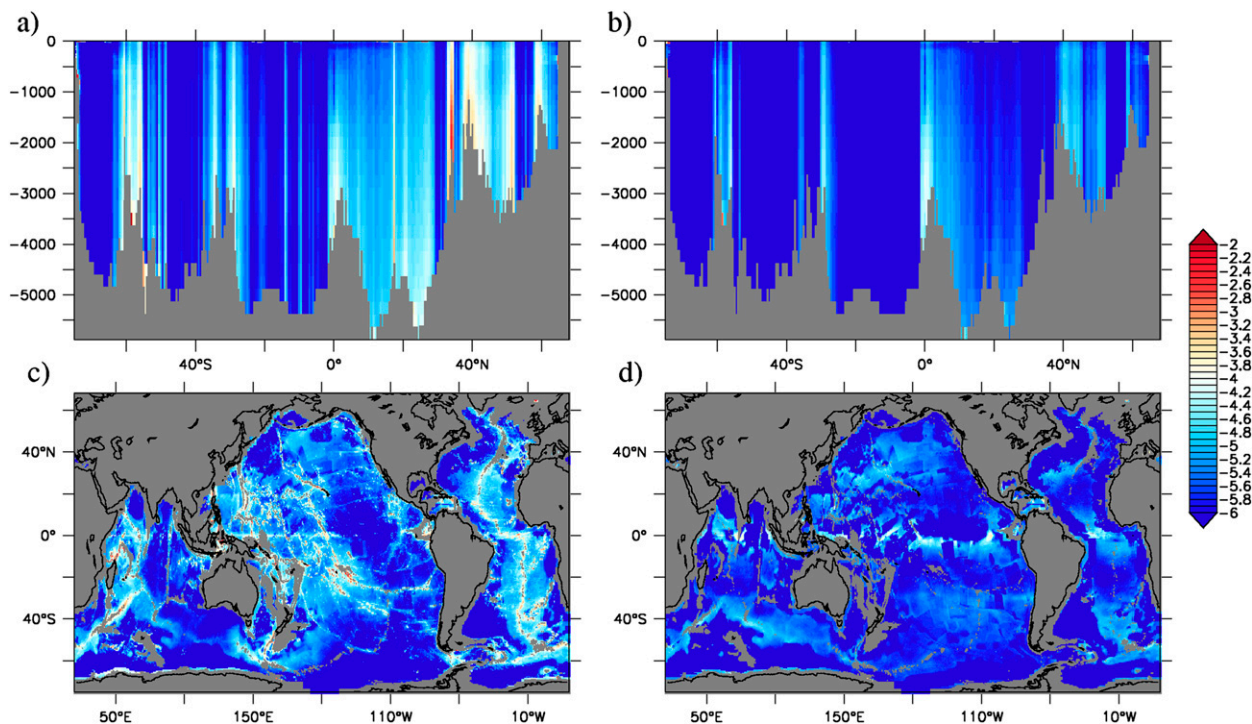


FIG. 6. Vertical diffusivity K at (top) 30°W and (bottom) 2800-m depth [$\log_{10}K$ (m^2s^{-1}) $^{-1}$] in the experiment with the (a),(c) M_2 compartment and the (b),(d) near-inertial wave compartment coupled to the wave continuum.

Mixing (IDEMIX) model by [Olbers and Eden \(2013\)](#) simplifies the problem by considering energy compartments integrated in wavenumber space for upward- and downward-propagating waves. The effect of nonlinear wave–wave interactions can then be accounted for by a few but reasonable assumptions. On the other hand, model parameters such as the time scale for vertical symmetrization of the wave field certainly depend on the unresolved distribution of energy in wavenumber space. Therefore, we extended the model by [Olbers and Eden](#)

(2013) through energy compartments representing the first few vertical modes of long gravity waves, such as internal tides and near-inertial waves, in addition to a compartment at higher vertical wavenumbers representing the wave continuum. While for the latter horizontal isotropy in wavenumber space can be assumed [although the compartment still depends on space in a Wentzel–Kramers–Brillouin (WKB) sense], the low-mode compartments are horizontally resolved both in physical and wavenumber space.

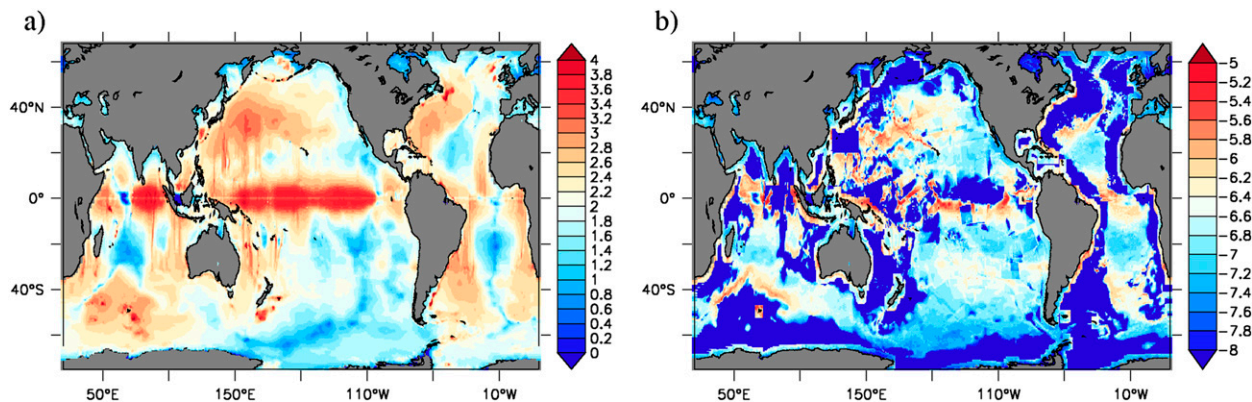


FIG. 7. Near-inertial wave energy E_{niw} [$\log_{10} \int_0^{2\pi} E_{\text{niw}} d\phi$ (J m^{-2}) $^{-1}$] and dissipation by scattering at rough topography $\int_0^{2\pi} T_{\text{niw}} d\phi$ [$\log_{10} F$ (m^3s^{-3}) $^{-1}$].

For the important specification of the interaction between the energy compartments, we use to a large extent analytical considerations. The effect of nonlinear triad interactions of a spectral peak, representing the internal tide or near-inertial waves, with the background continuum is derived directly from the respective scattering integral containing all triad interactions. The energy transfer from the low-mode compartment to the continuum derived from the scattering integral is quadratic, that is, it depends on the product of energies of both compartments. While the associated time scale is larger than 100 days for the near-inertial wave compartment, it becomes small equatorward of about 28° latitude for the M_2 tide due to parametric subharmonic instabilities. In fact, it becomes smaller than the tidal frequency, such that the weak interaction assumption begins to break down. Nevertheless, we use this theoretical result for our model, since it will at least qualitatively describe what happens for large amplitudes and strong wave–wave interactions for the parametric subharmonic instabilities. MacKinnon and Winters (2005) and Simmons (2008) describe the effect of parametric subharmonic instability in numerical simulations, and evidence for increased dissipation of internal waves equatorward of about 28° latitude is given by Hibiya and Nagasawa (2004) and MacKinnon et al. (2013). We emphasize that the instability works according to our analysis in the entire latitudinal band from 28.8°S to 28.8°N and not only at the critical latitude as speculated by MacKinnon et al. (2013).

It is appropriate here to point out some discrepancies with previous work on the nonlinear tidal decay. The interaction of a spectral peak with the background wave continuum has been investigated in several studies in the past (Olbers 1974; Pomphrey et al. 1980; Olbers and Pomphrey 1981). We stress that the results of these studies must be seen rather critically. The calculation of Olbers and Pomphrey (1981) is given for a latitude of 30° where the parametric subharmonic instability interactions of the M_2 tidal frequency are not possible, missing thus the most important interaction. Scaling of the results to lower latitudes, as discussed in Olbers and Pomphrey (1981) and in Olbers (1983), is therefore not valid. Furthermore, Olbers (1974) uses a rather unrealistic box-shaped model spectrum (GM72) of the background internal wave field, while Pomphrey et al. (1980) use a more realistic spectral shape, but apply a quite severe cutoff with respect to high vertical wavenumbers that are allowed to interact with the tide. The cutoff wavenumber used by Pomphrey et al. (1980) corresponds to 0.035 m^{-1} , which is far from the dissipation

cutoff wavenumber of $m_c = 1\text{ m}^{-1}$ of the realistic background spectra (Munk 1981). In fact, our new calculations using a realistic spectrum with much larger, more realistic cutoff wavenumbers yield very different results (see appendix). For a more detailed discussion of the mathematical treatment of the interaction in a random gravity wave field, we refer the reader to Olbers et al. (2012).

A further important interaction is due to the scattering of low-mode energy to the wave continuum by rough topography. This effect is linear in the energy of the low-mode compartment and analyzed in detail by Müller and Xu (1992). Since the decay time scale is proportional to the variance and mean wavenumber of the topography, recent estimates of the corresponding geophysical parameters of the abyssal hills given by Goff and Arbic (2010) can be used for this process. No comprehensive theory is at hand for the scattering of low-mode energy to the wave continuum at topographic obstacles of larger scale such as continental margins and isolated islands. We thus simply account for this effect through a reasonable constant linear decay time scale in the vicinity of the coastline.

Kelly et al. (2013) recently suggested that most of the low-mode internal M_2 tidal energy is dissipated at continental margins. In contrast, we find in this study that this process is less important compared to two other processes, that is, the parametric subharmonic instability of the internal low-mode M_2 tide in the presence of the wave continuum, and the scattering of internal M_2 tides to the wave continuum over rough topography. The latter process is estimated by Kelly et al. (2013) to be less important, while parametric subharmonic instability was ignored by these authors. The reason for the discrepancy with respect to topographic interactions is most likely that Kelly et al. (2013) use linear theory to assess the effect of rough topography in the interior, while in the present study weak nonlinear interactions at the topography are considered. Unlike the other two processes, the effect of scattering at the continental margins depends in our model on an ad hoc decay time scale, which we prescribed as 7 days. Using a time scale of 3 or 0.5 days instead of 7 days, however, increases the effect relative to the interior scattering only by a few percent, such that our choice of time scale already provides nearly an upper bound of the effect.

We finally note that the development of the IDEMIX model is not yet complete. We have not accounted for other tidal constituents, although this could be easily done. More important to the future development are missing forcing functions such as lee-wave generation by mesoscale eddies or the mean flow (e.g., Nikurashin

and Ferrari 2011), dissipation of balanced flows (Molemaker et al. 2010), or the forcing by surface waves (Olbers and Herterich 1979). The decomposition of the forcing functions as separate fluxes into the different energy compartments including their wave direction also has to be quantified. Furthermore, we have ignored the effect of the mean flow and mesoscale eddies in shaping the wave-supporting environment of gravity waves (e.g., Zhai et al. 2007), the scattering and interaction of gravity waves with the balanced flow (Polzin 2010), and changes in the dynamics of the wave field toward the tropics.

Acknowledgments. The authors thank Jonas Nycander and Saeed Falahat for sharing the tidal forcing data with us.

$$\begin{aligned} \lambda(\mathbf{K}) &= \int d^3 K_1 \\ &\times \int d^3 K_2 [T^+ \delta(\mathbf{K} - \mathbf{K}_1 - \mathbf{K}_2) \delta(\omega - \omega_1 - \omega_2) (\mathcal{A}_1 + \mathcal{A}_2) + 2T^- \delta(\mathbf{K} - \mathbf{K}_1 + \mathbf{K}_2) \delta(\omega - \omega_1 + \omega_2) (\mathcal{A}_2 - \mathcal{A}_1)] \\ &= \lambda^+ + \lambda^-, \end{aligned} \tag{A1}$$

where $\mathcal{A}(\mathbf{K}) = \mathcal{E}(\mathbf{K})/\omega$ is the action, and \mathcal{E} is the spectral density of the background continuum. The terms T^+ and T^- denote the cross section of triad wave-wave interactions, which is given in Olbers (1976). The first term λ^+ is usually called the sum interaction ($\omega = \omega_1 + \omega_2$, $\omega > \omega_1, \omega_2$) and is positive definite. It contributes to λ only for $\omega > 2f$ and is prone to PSI of the wave \mathbf{K} . For M_2 this occurs equatorward of 28.8° latitude. The second term λ^- is usually called the difference interaction ($\omega = \omega_1 - \omega_2$, $\omega < \omega_1, \omega_2$) and contributes to λ for all frequencies but may become negative. For M_2 it operates up to 74.5° latitude, where the M_2 tide ceases to exist as a freely propagating wave.

We have evaluated the Langevin rates of the sum and the difference interaction, respectively, for a model spectrum of the background continuum that is of a stripped GM76 form: the small inertial cusp in GM76 (see, e.g., Munk 1981; Olbers and Eden 2013) is omitted, and the frequency dependence is replaced by $B(\omega) = n_B f / \omega^2$ that is normalized to one with $n_B = (1 - f/N)^{-1}$. The integrals are evaluated in (k_1, ω_1) space after elimination of the δ functions in Eq. (A1).

The evaluation of the integrals in Eq. (A1) turns out to be quite cumbersome. First, the domain of integration is complicated (an example is shown in Fig. A1). Second, the integrand becomes singular on the boundaries of the domain, requiring a combination of analytical and

APPENDIX

Derivation of the Interaction Coefficients

a. Wave-wave interaction

We revisit in this appendix the interaction of a spectral peak (or line), such as a peak at the tidal M_2 frequency or a marked near-inertial peak, on top of the continuous part of the spectrum of gravity waves. For a detailed discussion of the mathematical treatment of the interaction in a random gravity field, we refer to Olbers et al. (2012). The decay of the energy density $\mathcal{E}_{\text{line}}$ in the spectral line with three-dimensional wavevector \mathbf{K} is governed by $\partial_t \mathcal{E}_{\text{line}} = -\lambda \mathcal{E}_{\text{line}}$ (plus other terms that we neglect here), where λ is the Langevin rate (see, e.g., Pomphrey et al. 1980; Müller et al. 1986). This rate is given by

numerical integration. Third, the integral is dominated by the behavior in small domains in (k_1, ω_1) space. Figure A1a shows the logarithm of the modulus of the integrand for the difference interactions related to λ^- and for the interaction of a spectral peak of vertical mode one and ω equal to the M_2 tidal frequency with the downward-propagating waves in the background continuum at a latitude of 20° . The integrand becomes zero along the blue valley in the figure centered at $\log k_1/k = 0$; it is negative to the left (smaller k_1) of this valley and positive to the right (larger k_1). In areas of negative integrand, the background continuum feeds energy into the spectral peak. This occurs primarily by a PSI mechanism at the background frequencies $\omega_1 = 2\omega$, visible by the tongue of the integration domain extending along $\omega_1 = 2\omega$ toward vanishing k_1 . Note that the cross section is small for the corresponding PSI triads; it decreases with frequency and increases with wavenumber. What makes the transfer efficient large is the large energy content at $\omega_1 = 2\omega$ in the continuum. Nevertheless, for low modes there is still a net loss of the energy of the spectral peak (see Fig. A2a). For higher modes, and higher than tidal frequencies, λ^- becomes negative, but the shift from positive to negative values strongly depends on the shape of the background spectrum in frequency and wavenumber space.

Figure A1b shows the logarithm of the integrand for the sum interaction related to λ^+ , again for M_2 and mode

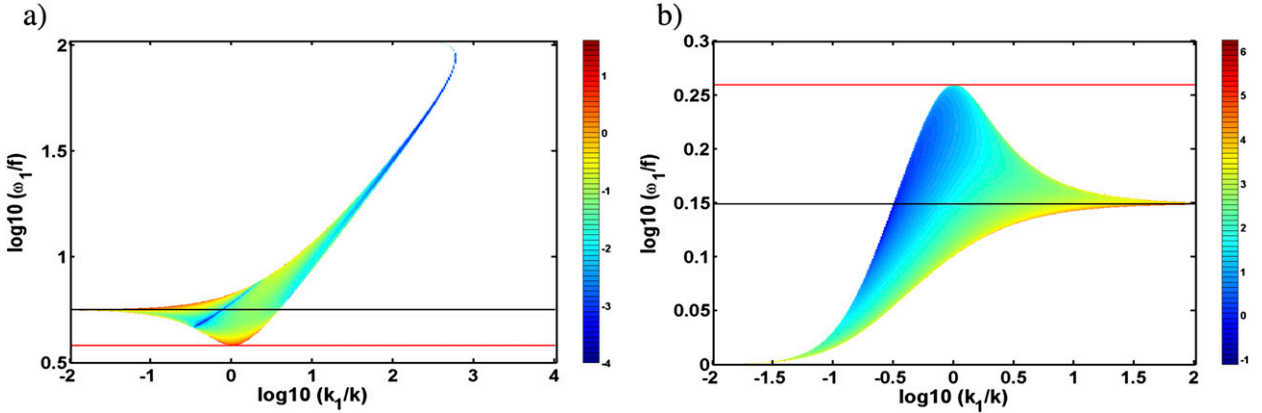


FIG. A1. (a) The logarithm of the absolute value of the integrand of the difference interaction related to the Langevin rate λ^- in Eq. (11) as a function of k_1/k and ω_1/f for an interaction of a spectral peak of vertical mode one and ω equal to the M_2 tidal frequency with downward-propagating waves in the background continuum at latitude 20° and $N = 5.25 \times 10^{-3} \text{ s}^{-1}$ [k_2 and ω_2 are given by the arguments of the δ functions in Eq. (11)]. (b) As in (a), but for the integrand for the sum interaction related to λ^+ . The straight lines in (a) denote $\omega_1 = \omega + f$ (red) and $\omega_1 = 2\omega$ (black). In (b), the lines denote $\omega_1 = \omega/2$ (black) and $\omega_1 = \omega - f$ (red).

one at 20° . It is always positive, which means that the spectral peak is losing energy. The energy is transferred to higher wavenumbers in the continuum for all frequencies ω_1 , occurring, however, very concentrated at frequencies around $\omega_1 = \omega/2$, where the integration domain extends in k_1 to infinity. This is again a PSI instability of the internal tide. The evaluation of the integral for λ^+ becomes problematic because the infinite integration interval at $\omega_1 = \omega/2$ picks up the high-wavenumber dependence of the spectrum, and in fact, λ^+ is mostly determined by the high-wavenumber cutoff of the spectrum (the cross-section T^+ increases with wavenumber and the wavenumber spectrum of GM76 does not fall off strongly enough). Using the usual (vertical) wavenumber cutoff of GM76 at $m_c = 1 \text{ m}^{-1}$,

the rate λ^+ becomes very large, implying decay times less than the tidal period. We stress that the weak-interaction assumption is therefore in principle violated for the interaction of M_2 with the very high wavenumbers in the background spectrum. In previous estimates of this wave–wave interaction, this was not noted because of either using the unrealistic background spectrum GM72 (Olbers 1974) or a quite small cutoff wavenumber (Pomphrey et al. 1980).

The decay rate corresponding to the difference interaction rate λ^- for the first mode is shown as a function of latitude in Fig. A2a and four values for N . The corresponding time scale ranges roughly between 10 and 100 days; thus, it is quite slow. The decay times for mode two and three are slightly smaller. The situation changes

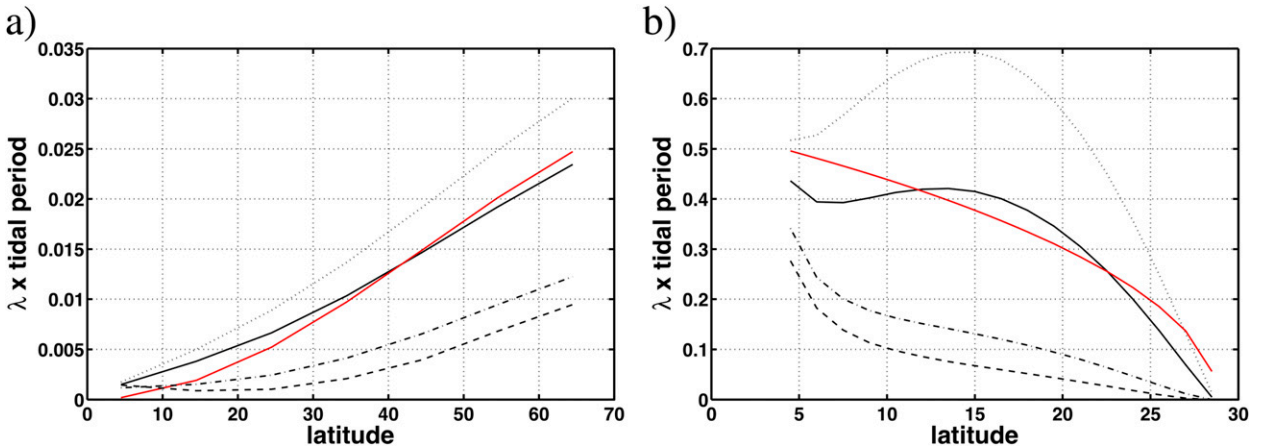


FIG. A2. Decay rates (times the tidal period) related to (a) λ^- and (b) λ^+ for the M_2 tide of mode one as a function of latitude, interacting with the background continuum. Four values of N are used: $N = (0.75, 1, 2, 3) \times 5.25 \times 10^{-3} \text{ s}^{-1}$ as dotted, solid, dashed–dotted, and dashed lines, respectively. The cutoff wavenumber of the continuum spectrum is $3 \times m_\star = 0.03 \text{ m}^{-1}$. The red line is an approximation to the solid black line, as explained in the text.

drastically when considering the sum interaction rate λ^+ (Fig. A2b). We have calculated λ^+ for different spectral cutoffs, ranging from $3 \times m_\star$ —comparable to the cutoff used in Pomphrey et al. (1980)—to $100 \times m_\star = 1 \text{ m}^{-1}$, which is the appropriate cutoff for the spectrum GM76 (Cairns and Williams 1976; Munk 1981) (here $m_\star = 0.01 \text{ m}^{-1}$ is the spectral bandwidth of GM76). For all cutoffs the energy content of the background spectrum is adjusted to the same value of $3 \times 10^{-3} \text{ m}^2 \text{ s}^{-2}$. We found that except for the range of very severe cutoffs the decay time scales are less than the M_2 tidal period. The weak interaction assumption begins therefore to break down for the PSI interactions with the very high wavenumbers in the background spectrum. Nevertheless, the analysis indicates what happens: The energy in the spectral peak decreases much stronger compared to higher latitudes (north of the critical latitude), where the decay of the peak comes only from the difference interactions. Figure A2b shows λ^+ for a cutoff at $3 \times m_\star = 0.03 \text{ m}^{-1}$, similar to what Pomphrey et al. (1980) used and what we also implement in the present model.

The relation between the decay rate λ and the coupling coefficient α_{M_2-c} appearing in Eq. (7) is derived as follows. First, we have $\int \lambda \mathcal{E}_{\text{line}} dz = \alpha_{M_2-c} E_{M_2} \int E_c dz$ for the vertically integrated exchange of the spectral peak and the continuum, where $\lambda = \lambda^+ + \lambda^-$. Some approximations are necessary concerning the vertical integrations on both sides. Since λ is proportional to the energy E_c of the continuum [see Eq. (11)], we express the decay rates for sum and difference interaction in the form $\lambda^\pm(N, \phi) = \beta^\pm(N) g^\pm(\phi) E_c$, where ϕ denotes latitude. A reasonable approximation of the dependency $\lambda^\pm(N, \phi)$ for the first mode (see Fig. A2) is achieved with $\beta^\pm(N) = \beta_0^\pm(N_0/N)$, where N is the actual local Brunt–Väisälä frequency in the respective simulation, $N_0 = 5.25 \times 10^{-3} \text{ s}^{-1}$ is the standard value, and $g^+(\phi) = [\sin(\phi_s - \phi)/\sin(\phi_s)]^{1/2}$, $g^+ = 0$ for $\phi > \phi_s$, and $g^-(\phi) = [\sin(\phi)/\sin(\phi_n)]^2$ with $\phi_s = 28.8^\circ$ and $\phi_n = 74.5^\circ$. The coefficients are

$\beta_0^+ = 4 \times 10^{-3} \text{ s m}^{-2}$ and $\beta_0^- = 2 \times 10^{-4} \text{ s m}^{-2}$, and the approximation is shown in Fig. A2 (red curves). Our approximation to λ^\pm can certainly be improved, in particular for complicated patterns in λ^+ , but we regard it as sufficient for our purpose and use it in our model. Approximating $\int \lambda^\pm \mathcal{E}_{\text{line}} dz \simeq E_{M_2} \int \lambda^\pm dz \simeq \beta_0^\pm(N_0/\bar{N}) \int E_c dz$ with a depth-averaged value \bar{N} , we finally arrive at

$$\alpha_{M_2-c} = [\beta_0^+ g^+(\phi) + \beta_0^- g^-(\phi)] N_0 / \bar{N}. \quad (\text{A2})$$

We have also evaluated the decay time for near-inertial waves. Since only the difference interaction is possible for this frequency, decay time scales are large on the order of 100 days and longer, which we thus do not consider further.

b. Wave–topography interaction

Müller and Xu (1992) discuss the redistribution of energy in horizontal wavenumber space of internal waves impinging and scattering on rough bottom topography. They find that for low frequencies, a significant amount of incoming energy is transferred from low to high horizontal wavenumbers (cf. their Fig. 2). Considering an expansion of the scattered waves and the bottom boundary conditions for small ratios of topography height to vertical wavelengths and topographic slopes to waves slopes up to third order, they derive an expression for the energy flux at the bottom given by

$$F_i(\mathbf{k}, m) + F_s(\mathbf{k}, -m) = \Phi(\mathbf{k}, m), \quad z = -h, \quad (\text{A3})$$

where m is the vertical wavenumber, F_i is the incoming downward energy flux with positive m , and F_s is the upward scattered energy flux with negative m . The flux Φ transfers energy from one location in wavenumber space to another. Müller and Xu (1992) show that Φ becomes, written as density in (\mathbf{k}, ω) space,

$$\Phi(\mathbf{k}, \omega) = \int T(\mathbf{k}, \mathbf{k}') S(\mathbf{k} - \mathbf{k}') [\mathcal{E}^-(\mathbf{k}') V(\omega)/|\mathbf{k}'| - \mathcal{E}^-(\mathbf{k}) V(\omega)/|\mathbf{k}|] d\mathbf{k}', \quad (\text{A4})$$

where $S(\mathbf{k}, \mathbf{x})$ and $\mathcal{E}^-(\mathbf{k}, \omega, \mathbf{x}, z = -h, t)$ denote the spectrum of the topography and the energy spectrum of the downward incoming waves at the bottom, respectively. The scattering cross section is given by

$$T(\mathbf{k}, \mathbf{k}') = 2 \frac{N^2 - \omega^2}{\omega^2 - f^2} |\mathbf{k}| |\mathbf{k}'| \left(\cos^2 \gamma + \frac{f^2}{\omega^2} \sin^2 \gamma \right),$$

$$V(\omega) = \frac{(\omega^2 - f^2)^{3/2} (N^2 - \omega^2)^{1/2}}{\omega(N^2 - f^2)}, \quad (\text{A5})$$

where γ is the angle between the horizontal wavevectors \mathbf{k} and \mathbf{k}' . The first term in brackets in Eq. (A4) is a gain of energy at \mathbf{k} due to the scattering of energy from other wavenumbers, and the second is a loss due to the scattering of energy at \mathbf{k} to other wavenumbers. We are interested in the latter. It was shown by Müller and Xu (1992) that this energy flux can be written to a good approximation as

$$\begin{aligned} & \int T(\mathbf{k}, \mathbf{k}') S(\mathbf{k} - \mathbf{k}') \mathcal{E}^- V / |\mathbf{k}| d\mathbf{k}' \\ & \approx \frac{N^2 - \omega^2}{\omega^2 - f^2} \left(1 + \frac{f^2}{\omega^2} \right) V \mathcal{E}^- h_{\text{rms}}^2 \bar{k}, \end{aligned} \quad (\text{A6})$$

with the total variance of topographic variations $h_{\text{rms}}^2 = \int S(\mathbf{k}) dk$ and the mean topographic wavenumber $\bar{k} = h_{\text{rms}}^{-2} \int |\mathbf{k}| S(\mathbf{k}) dk$.

To connect this energy flux at the bottom to our model, we consider for the moment the low-mode compartments similar to the wave compartment as composed of the sum of the energies of the upward- and downward-propagating waves \mathcal{E}_n^+ and \mathcal{E}_n^- . The total energy $\mathcal{E}_n = \mathcal{E}_n^+ + \mathcal{E}_n^-$ is related to the modal energy E_n of the low modes by $\mathcal{E}_n = E_n \Phi$, with the structure function $\Phi(z)$ given by Eq. (5). Instead of \mathcal{E}_n , however, we need \mathcal{E}_n^- in Eq. (A6). To close the model we must assume approximate symmetry in upward- and downward-propagating waves at the bottom, that is, $2\mathcal{E}_n^- = \mathcal{E}_n = E_n \Phi$ at $z = -h$. Similar to the wave continuum, the flux given by Eq. (A6) enters as boundary condition for the vertical refraction term for the radiative transfer equation for \mathcal{E}_n . The flux therefore shows up as a forcing in the vertically integrated, radiative transfer equation for $\int \mathcal{E}_n dz$, which is identical to Eq. (2). We therefore simply add the flux given by Eq. (A6) as T_n in Eq. (2). With $\phi_n' = 0$ and $\phi_n^2/c_n^2 \approx 2/h$ at $z = -h$, the term T_n finally becomes

$$\begin{aligned} T_n &= -\tau_n^{-1} E_n, \\ \tau_n^{-1} &= \frac{1}{2h} \left(1 + \frac{f^2}{\omega^2} \right)^2 \frac{(N^2 - \omega^2)^{3/2} (\omega^2 - f^2)^{1/2}}{\omega(N^2 - f^2)} h_{\text{rms}}^2 \bar{k}. \end{aligned} \quad (\text{A7})$$

The frequency ω is either specified as the tidal frequency or the near-inertial frequency $1.05f$. Equation (17) can be written as

$$\tau_n^{-1} = \frac{1}{2h} \left(1 + \frac{f^2}{\omega^2} \right)^2 m |\mathbf{c}_g| h_{\text{rms}}^2 \bar{k}, \quad (\text{A8})$$

with the horizontal group velocity \mathbf{c}_g of internal gravity waves and vertical wavenumber m . In the numerical code, we use the long-wave expression from Eq. (3) for \mathbf{c}_g and the vertical wavenumber $m = n\pi/h$.

The impact of topography on the scattering flux is described by the total variance of topographic h_{rms}^2 and the mean wavenumber of the spectrum \bar{k} . We use the digital maps of geophysical parameters for the abyssal hills given by Goff and Arbic (2010) for h_{rms}^2 and $\bar{k} = 2\pi/\lambda_n$, where λ_n is the characteristic width and h_{rms} is the rms topographic height. These maps are based on estimates of paleo-spreading rates of the midoceanic

ridge system and sediment thickness and are shown and discussed in Goff and Arbic (2010, their Figs. 5 and 6). Following Goff and Arbic (2010), we use a linear relation between spreading rates r and uncorrected rms height h_0 and width λ_0 , that is, $h_0 = -r \times 1473.4 y + 247 \text{ m}$ and $\lambda_0 = -r \times 43\,900 y + 7444 \text{ m}$. The correction due to sedimentation is applied by converting to the actual values of h_{rms} and λ_n by

$$\begin{aligned} h_{\text{rms}} &= \begin{cases} h_0 - S/2 & \text{for } S/2 < h_0 \\ 0 & \text{for } S/2 \geq h_0 \end{cases}, \\ \lambda_n &= \lambda_0 + 1.3\lambda_0 S/h_0, \end{aligned} \quad (\text{A9})$$

where S denotes the sediment thickness. Spreading rates r have been downloaded from data available online (from <http://www.earthbyte.org/Resources/agegrid2008.html> and sediment thickness S is provided at <http://www.ngdc.noaa.gov/mgg/sedthick>).

REFERENCES

- Alford, M. H., and Z. Zhao, 2007: Global patterns of low-mode internal-wave propagation. Part I: Energy and energy flux. *J. Phys. Oceanogr.*, **37**, 1829–1848, doi:10.1175/JPO3085.1.
- Cairns, J. L., and G. O. Williams, 1976: Internal wave observations from a midwater float, 2. *J. Geophys. Res.*, **81**, 1943–1950, doi:10.1029/JC081i012p01943.
- Furuichi, N., T. Hibiya, and Y. Niwa, 2008: Model-predicted distribution of wind-induced internal wave energy in the world's oceans. *J. Geophys. Res.*, **113**, C09034, doi:10.1029/2008JC004768.
- Garrett, C., 2001: What is the near-inertial wave band and why is it different from the rest of the internal wave spectrum? *J. Phys. Oceanogr.*, **31**, 962–971, doi:10.1175/1520-0485(2001)031<0962:WITNIB>2.0.CO;2.
- Goff, J. A., and B. K. Arbic, 2010: Global prediction of abyssal hill roughness statistics for use in ocean models from digital maps of paleo-spreading rate, paleo-ridge orientation, and sediment thickness. *Ocean Modell.*, **32**, 36–43, doi:10.1016/j.ocemod.2009.10.001.
- Gouretski, V., and K. Koltermann, 2004: WOCE global hydrographic climatology. *Berichte des BSH* 55, 52 pp.
- Gregg, M. C., 1989: Scaling turbulent dissipation in the thermocline. *J. Geophys. Res.*, **94**, 9686–9698, doi:10.1029/JC094iC07p09686.
- Hasselmann, K., 1968: Weak-interaction theory of ocean waves. *Basic Dev. Fluid Dyn.*, **2**, 117–182, doi:10.1016/B978-0-12-395520-3.50008-6.
- Hibiya, T., and M. Nagasawa, 2004: Latitudinal dependence of diapycnal diffusivity in the thermocline estimated using a finescale parameterization. *Geophys. Res. Lett.*, **31**, L01301, doi:10.1029/2003GL017998.
- Jayne, S., 2009: The impact of abyssal mixing parameterizations in an ocean general circulation model. *J. Phys. Oceanogr.*, **39**, 1756–1775, doi:10.1175/2009JPO4085.1.
- Jochum, M., B. P. Briegleb, G. Danabasoglu, W. G. Large, N. J. Norton, S. R. Jayne, M. H. Alford, and F. O. Bryan, 2013: The impact of oceanic near-inertial waves on climate. *J. Climate*, **26**, 2833–2844, doi:10.1175/JCLI-D-12-00181.1.
- Kelly, S., N. Jones, J. Nash, and A. Waterhouse, 2013: The geography of semidiurnal mode-1 internal-tide energy loss. *Geophys. Res. Lett.*, **40**, 4689–4693, doi:10.1002/grl.50872.

- Kunze, E., and S. L. Smith, 2004: The role of small-scale topography in turbulent mixing of the global ocean. *Oceanography*, **17**, 55–64, doi:10.5670/oceanog.2004.67.
- Large, W., and G. Crawford, 1995: Observations and simulations of upper-ocean response to wind events during the ocean storms experiment. *J. Phys. Oceanogr.*, **25**, 2831–2852, doi:10.1175/1520-0485(1995)025<2831:OASOUO>2.0.CO;2.
- MacKinnon, J., and K. Winters, 2005: Subtropical catastrophe: Significant loss of low-mode tidal energy at 28.9°. *Geophys. Res. Lett.*, **32**, L15605, doi:10.1029/2005GL023376.
- , M. H. Alford, O. Sun, R. Pinkel, Z. Zhao, and J. Klymak, 2013: Parametric subharmonic instability of the internal tide at 29°N. *J. Phys. Oceanogr.*, **43**, 17–28, doi:10.1175/JPO-D-11-0108.1.
- Marshall, J., A. Adcroft, C. Hill, L. Perelman, and C. Heisey, 1997: A finite-volume, incompressible Navier Stokes model for studies of the ocean on parallel computers. *J. Geophys. Res.*, **102**, 5753–5766, doi:10.1029/96JC02775.
- McComas, C., and P. Müller, 1981: Time scales of resonant interactions among oceanic internal waves. *J. Phys. Oceanogr.*, **11**, 139–147, doi:10.1175/1520-0485(1981)011<0139:TSORIA>2.0.CO;2.
- Molemaker, M. J., J. C. McWilliams, and X. Capet, 2010: Balanced and unbalanced routes to dissipation in an equilibrated Eady flow. *J. Fluid Mech.*, **654**, 35–63, doi:10.1017/S0022112009993272.
- Müller, M., J. Cherniawsky, M. Foreman, and J.-S. Storch, 2012: Global M_2 internal tide and its seasonal variability from high resolution ocean circulation and tide modeling. *Geophys. Res. Lett.*, **39**, L19607, doi:10.1029/2012GL053320.
- Müller, P., and N. Xu, 1992: Scattering of oceanic internal gravity waves off random bottom topography. *J. Phys. Oceanogr.*, **22**, 474–488, doi:10.1175/1520-0485(1992)022<0474:SOOIGW>2.0.CO;2.
- , and M. Briscoe, 1999: Diapycnal mixing and internal waves. *Dynamics of Oceanic Internal Gravity Waves: Proc. 11th 'Aha Huliko'a Hawaiian Winter Workshop*, Honolulu, HI, University of Hawai'i at Mānoa, 289–294.
- , and A. Natarov, 2003: The internal wave action model (IWAM). *Near-Boundary Processes and Their Parameterization: Proc. 13th 'Aha Huliko'a Hawaiian Winter Workshop*, Honolulu, HI, University of Hawai'i at Mānoa, 95–105.
- , G. Holloway, F. Henyey, and N. Pomphrey, 1986: Nonlinear interactions among internal gravity waves. *Rev. Geophys.*, **24**, 493–536, doi:10.1029/RG024i003p00493.
- Munk, W., 1981: Internal waves and small-scale processes. *Evolution of Physical Oceanography*, B. A. Warren and C. Wunsch, Eds., MIT Press, 264–291.
- Nikurashin, M., and R. Ferrari, 2011: Global energy conversion rate from geostrophic flows into internal lee waves in the deep ocean. *Geophys. Res. Lett.*, **38**, L08610, doi:10.1029/2011GL046576.
- Nycander, J., 2005: Generation of internal waves in the deep ocean by tides. *J. Geophys. Res.*, **110**, C10028, doi:10.1029/2004JC002487.
- Olbers, D. J., 1974: *On the Energy Balance of Small-Scale Internal Waves in the Deep Sea*. *Hamb. Geophys. Einzelschriften*, No. 24, G. M. L. Wittenborn, 91 pp.
- , 1976: Nonlinear energy transfer and the energy balance of the internal wave field in the deep ocean. *J. Fluid Mech.*, **74**, 375–399, doi:10.1017/S0022112076001857.
- , 1983: Models of the oceanic internal wave field. *Rev. Geophys. Space Phys.*, **21**, 1567–1606, doi:10.1029/RG021i007p01567.
- , and K. Herterich, 1979: The spectral energy transfer from surface waves to internal waves. *J. Fluid Mech.*, **92**, 349–379, doi:10.1017/S0022112079000653.
- , and N. Pomphrey, 1981: Disqualifying two candidates for the energy balance of the oceanic internal wave field. *J. Phys. Oceanogr.*, **11**, 1423–1425, doi:10.1175/1520-0485(1981)011<1423:DTCFTE>2.0.CO;2.
- , and C. Eden, 2013: A global model for the diapycnal diffusivity induced by internal gravity waves. *J. Phys. Oceanogr.*, **43**, 1759–1779, doi:10.1175/JPO-D-12-0207.1.
- , J. Willebrand, and C. Eden, 2012: *Ocean Dynamics*. Springer, 704 pp.
- Osborn, T. R., and C. S. Cox, 1972: Oceanic fine structure. *Geophys. Astrophys. Fluid Dyn.*, **3**, 321–345, doi:10.1080/03091927208236085.
- Polzin, K. L., 2010: Mesoscale eddy-internal wave coupling. Part II: Energetics and results from POLYMODE. *J. Phys. Oceanogr.*, **40**, 789–801, doi:10.1175/2009JPO4039.1.
- Pomphrey, N., J. D. Meiss, and K. M. Watson, 1980: Description of nonlinear internal wave interactions using Langevin methods. *J. Geophys. Res.*, **85**, 1085–1094, doi:10.1029/JC085iC02p01085.
- Rimac, A., J.-S. von Storch, C. Eden, and H. Haak, 2013: The influence of high-resolution wind stress field on the power input to near-inertial motions in the ocean. *Geophys. Res. Lett.*, **40**, 4882–4886, doi:10.1002/grl.50929.
- Simmons, H. L., 2008: Spectral modification and geographic redistribution of the semi-diurnal internal tide. *Ocean Modell.*, **21**, 126–138, doi:10.1016/j.ocemod.2008.01.002.
- St. Laurent, L., and C. Garrett, 2002: The role of internal tides in mixing the deep ocean. *J. Phys. Oceanogr.*, **32**, 2882–2899, doi:10.1175/1520-0485(2002)032<2882:TROITI>2.0.CO;2.
- , M. H. Alford, and T. Paluszkiwicz, 2012: An introduction to the special issue on internal waves. *Oceanography*, **25**, 15–19, doi:10.5670/oceanog.2012.37.
- Wunsch, C., and R. Ferrari, 2004: Vertical mixing, energy and the general circulation of the oceans. *Annu. Rev. Fluid Mech.*, **36**, 281–314, doi:10.1146/annurev.fluid.36.050802.122121.
- Zhai, X., R. J. Greatbatch, and C. Eden, 2007: Spreading of near-inertial energy in a $1/12^\circ$ model of the North Atlantic Ocean. *Geophys. Res. Lett.*, **34**, L10609, doi:10.1029/2007GL029895.